Case Studies in Thermal Engineering 61 (2024) 105021

Contents lists available at ScienceDirect

Case Studies in Thermal Engineering

journal homepage: www.elsevier.com/locate/csite

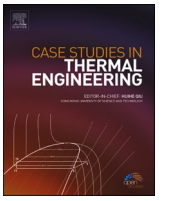

Direct coupling of pressurized gas receiver to a brayton supercritical CO_2 power cycle in solar thermal power plants

José Ignacio Linares [a,*], Eva Arenas [a,b], Maria José Montes [c], Alexis Cantizano [a,b], José Rubén Pérez-Domínguez [a], José Porras [a]

[a] Rafael Mariño Chair in New Energy Technologies, ICAI School of Engineering, Comillas Pontifical University, Alberto Aguilera 25, 28015, Madrid, Spain

[b] Institute for Research in Technology, ICAI School of Engineering Engineering, Comillas Pontifical University, Santa Cruz de Marcenado 26, 28015, Madrid, Spain

[c] Department of Energy Engineering, Universidad Nacional de Educación a Distancia (UNED), Juan del Rosal 12, 28040, Madrid, Spain

HIGHLIGHTS

- A supercritical CO_2 cycle has been directly coupled to a central solar receiver.
- Three layouts have been studied: recompression, intercooling, and partial cooling.
- The solar receiver consists of microchannel absorber panels in radial configuration.
- The solar tower plant has been sized to optimize the energy and exergy efficiency.
- LCOE is below 167 €/MWh, whereas overall efficiency ranges from 30.26 % to 31.58 %.

ARTICLE INFO

Keywords:
CSP
Supercritical CO_2 power cycle
Pressurized gas receiver
Microchannel receiver

ABSTRACT

Three layouts of Brayton supercritical CO_2 power cycles directly coupled to the receiver are proposed for Generation 3 solar power plants: conventional recompression, recompression with partial cooling, and recompression with intercooling. To achieve direct coupling, the solar heat is introduced downstream of the turbine, where CO_2 pressure is lower. A higher temperature rise diminishes the receiver's dimensions, thus increasing its energy efficiency. It also lowers the average working temperature since the maximum temperature is fixed at 700 °C, thereby reducing losses. However, optical efficiency decreases as the receiver size diminishes. Both intercooling and partial cooling layouts further increase the cycle's net efficiency, which reduces the receiver's size, following similar trends observed with an increase in temperature rise. Considering all these effects, various factors push in opposite directions, affecting overall efficiency and costs. This competitive interplay results in overall efficiencies ranging from 30.26 % to 31.58 % and Levelized Costs of Electricity (LCOEs) between 162.47 €/MWh and 166.81 €/MWh. In conclusion, similar outcomes in terms of energy and economics are achieved with the three layouts, suggesting the simplest layout (recompression) as the most advisable. If thermal storage is incorporated, partial cooling becomes preferable due to its significant increase in the receiver's temperature rise.

* Corresponding author.
E-mail address: linares@comillas.edu (J.I. Linares).

https://doi.org/10.1016/j.csite.2024.105021
Received 9 April 2024; Received in revised form 12 July 2024; Accepted 22 August 2024
Available online 23 August 2024

ACRONYMS

AC	Auxiliary Compressor
CAPEX	Capital Expenditure
CRS	Central Receiver System
CSP	Concentrating Solar Power
EES	Engineering Equation Solver
FCI	Fixed Capital Investment
G	Generator
HCE	Heat Control Elements
HTF	Heat Transfer Fluid
HTR	High Temperature Recuperator
IC	Intercooler
ICL	Intercooling Layout
IRENA	International Renewable Energy Agency
LCOE	Levelized Cost of Electricity
LTR	Low Temperature Recuperator
MC1	Main Compressor 1
MC2	Main Compressor 2
OFFSC	Off-Site Costs
OM	Operation and Maintenance
ONSC	On-Site Costs
OPEX	Operational Expenditure
PBT	Packed Bed Thermocline
PC	Precooler
PCHE	Printed Circuit Heat Exchanger
PCL	Partial Cooling Layout
PEC	Purchased-Equipment Costs
RC	Recompression layout
S-CO_2	Brayton power cycle with Supercritical CO_2
T	Turbine
TES	Thermal Energy Storage
TRM	Thermal Resistance Model

NOTATION

Latin letters

A	Heat transfer area
a	Escalation factor
C	Cost
$CELF$	Constant Escalation Levelization Factor
Cp	Specific heat at constant pressure
CRF	Capital Recovery Factor
Ex	Exergy
f	Friction factor, Correction factor
h	Convection coefficient
k	Thermal conductivity
L	Length
M	Magnitude
$\dot{m}$	Mass flow rate
N	Lifespan of the project
Nu	Nusselt number
p	Pressure
P	Annual electricity production
Pr	Prandtl number
q	Heat duty per unit mass
$\dot{Q}$	Heat duty
R	Thermal resistance
r	Nominal rate of escalation
Re	Reynolds number
s	Entropy
T	Temperature
$\overline{T}$	Average entropic temperature
t	Thickness
u	Velocity
v	Specific volume
W	Work
$\dot{W}$	Power
$wacc$	Weighted Average Capital Cost
ρ	Density

Greek letters

α	Mass flow rate ratio in the auxiliary compressor
η	Efficiency
δ	Relative heat rejection

Subscripts

0	Frontal, Reference

(*continued on next page*)

(*continued*)

A	Air
Abs	Absorbed
aIC	Air in the intercooler
aPC	Air in the precooler
c,conv	Convection between the channel base and top surface
Conv	Convection
conv,HTF	Convection to the HTF
D	Darcy
Dh	Hydraulic diameter
en, solar_field & receiver	Energy, solar field & receiver
en,receiver	Energy, receiver
ex, solar_field & receiver	Exergy, solar field & receiver
ex,receiver	Exergy, receiver
F	Fluid, Fanning, Fin
f,cond	Conduction through the fin half-length
f,conv	Convection from the fin surface to the fluid
heliostat_field	Heliostat field
HR	Heat rejection
HS	Heat supply
HTF,receiver	Heat transfer fluid in the receiver
ICfan	Intercooler fan
io	Inlet/outlet
Is	Inner Surface
Loss	Losses
loss, conv	Convection losses
loss,rad	Radiation losses
loss,ref	Reflection losses
MC1	Main compressor 1
MC2	Main compressor 2
net-cycle	Net Cycle
opt, solar_field	Optical, solar field
P	Plate; Pressure
p,cond	Conduction through the wall thickness of the intermediate (frontal) plate
PCfan	Fan of the precooler
rec	Receiver
solar	Radiation
solar, receiver	Radiation over the receiver
T	Turbine; Temperataure
th,HTF,receiver	Thermal energy supplied to the transfer fluid in the receiver
TMG	Set of turbomachines and generator
tower	Tower of the receiver
W	Width
Others	
||	Resistances in parallel

1. Introduction

The current energy context highlights the need for a sustainable, secure, and competitive energy supply, where Concentrating Solar Power (CSP) plants can play an important role. According to the International Renewable Energy Agency (IRENA) [1], the Levelized Cost of Electricity (LCOE) of CSP plants decreased from 358 $/MWhe in 2010 to 114 $/MWhe in 2022. Despite this reduction, the LCOE still represents a high value, posing a significant obstacle to the widespread adoption of this technology. The Spanish government plans to double its current CSP capacity by 2030 [2], supported by auctions. While the first auction did not allocate any CSP project [3], recent regulations have introduced additional non-economic criteria, including resilience, environmental sustainability, innovation, and socioeconomic impact [4]. These criteria could benefit CSP plants due to their ability to integrate thermal energy storage (TES), allowing dispatchability.

In this context, the most conventional TES option is indirect storage in molten salt tanks [5]. However, there are many studies focused on exploring alternative paths. For instance, Li et al. [6] and Trevisan [7] propose direct storage using a sensible-packed bed thermocline (PBT) for pressurized air; additionally, a novel approach within the thermocline concept [8] involves a system based on a matrix of small individual vessels to reduce wall thickness. Regarding energy storage materials, detailed analyses are needed to enhance understanding and performance. Sathishkumar and Cheralathan in Ref. [9] explore the phase transition performance of deionized water-based nano-enhanced phase change materials for cool thermal storage systems, and in Ref. [10], the same authors examine the impact of thermal resistance and time constant on the phase change properties of carbon flake-based materials.

A first attempt to improve the competitiveness of CSP plants would focus on cost reduction, primarily in investment and operation and maintenance (OM) costs. Nevertheless, another approach is to achieve higher overall efficiency values. The next generation of Concentrating Solar Power plants (CSP Gen3) is based on the integration of a Central Receiver System (CRS) with a supercritical CO_2 power cycle (S-CO_2). This combination aims to enhance overall plant performance, reduce the footprint, and provide operational flexibility while accommodating a variety range of thermal sources [11,12], and [13]. The integration of supercritical S-CO_2 power

cycles with CSP can reduce the LCOE by 15.6 %–67.7 % compared to current CSP technologies, as highlighted in a comprehensive review [12]. This work covers comparisons of CSP technologies, S-CO_2 properties and layouts, material degradation, and both thermodynamic and economic analyses.

In this context, several studies on S-CO_2 indirect cycles have emerged, comparing different layouts and optimizing key parameters to achieve optimal performance. Most of these layouts are based on the recompression concept. In Ref. [14], different recompression layouts are systematically compared, considering they are indirectly coupled to a central receiver system that uses advanced molten salts as Heat Transfer Fluid (HTF). Some of the results of this comparison, for a hot salt temperature between 600 °C and 800 °C, are summarized as follows: the intercooling cycle presents the highest efficiency; the intercooling and partial cooling are the most complex, as they incorporate two extra compressors and one extra intercooler, compared to the conventional recompression cycle; and, the partial cooling cycle presents the highest temperature difference in the primary heat exchanger, which leads to a reduced molten salt inventory. Further work [15] analyzes the overall performance of two CSP plants based on the recompression and partial cooling layouts. It concludes that while the recompression cycle has higher efficiency and is less complex than the partial cooling cycle, the CSP plant with partial cooling has a lower investment cost and generates more net electricity. This is due to its greater temperature difference in the primary heat exchanger, resulting in smaller storage tanks, higher receiver efficiencies, and lower pump consumption, as the molten salt flow rate is also lower. In summary, many factors affect the selection of a supercritical cycle layout, and this analysis must be tailored to each specific CSP plant configuration. Multi-objective optimizations, targeting system efficiency and specific work, indicate that cycle layouts such as intercooling and partial cooling perform better than recompression and precompression layouts. The simple recuperation cycle shows the poorest performance [14], aligning with similar findings in Ref. [16]. It has been found that thermal efficiency increases monotonically with the cycle temperature [17].

Other analyses emphasize the LCOE of different configurations. Partial cooling achieves a 6.2 % reduction compared to both the simple and the recompression cycles [15]. This reduction is due to factors such as a larger temperature difference in the primary heat exchanger and a colder average operating temperature of the receiver. Currently, multiple studies are examining system performance and the design parameters of key components. For example [18], concludes that doubling the pressure loss in pipe sections reduces power generation and power supply efficiencies by 3.290 % and 4.377 %, respectively. Several studies focus on the dynamic response of direct cycles to achieve sustained, fully supercritical operation. In Ref. [19], simulations are performed under varying ambient air temperatures and solar energy inputs for summer and winter, highlighting the importance of CO_2 charge manipulation and compressor inlet conditions. Meanwhile [20], analyzes the impact of the relative hot-to-cold side volume ratios.

The comparison presented in this paper is framed within another research line proposed for CSP Gen3, which involves the use of a pressurized gas as HTF in the solar receiver. Due to the ability of S-CO_2 to withstand higher operating temperatures than molten salts, direct cycles can achieve overall thermal efficiencies 1.5 % higher than those of indirect cycles [21]. Zhu et al. [22] demonstrate that the thermal and exergy efficiencies of direct cycles increase linearly as turbine inlet temperature rises.

Although it is difficult to identify the optimal HTF for the solar subsystem, the main advantages of gases are their low cost, high-temperature stability, absence of corrosion issues, and relatively easy coupling to an S-CO_2 cycle, either directly as proposed in this work or by using a Printed Circuit Heat Exchanger (PCHE). The main drawbacks of the gases are the limited heat transfer, the lack of a direct large-scale storage system, and the associated high-pressure drop. This pressure drop can be reduced using pressurized gas instead of atmospheric air in a volumetric receiver. Moreover, as pressurized gas circuits are closed systems, gases other than air can be used: CO_2, N_2, He, and Ar, which may present better thermophysical properties depending on the working conditions [23]. Finally, pressurized gases are also particularly suitable for compact geometries similar to those in compact heat exchangers, like the microchannel receiver used in this comparative study. The main advantage of this type of receiver is the reduction in the absorber surface area, which consequently decreases the solar field size and, therefore, its associated investment cost.

The state-of-the-art in solar receivers based on compact structures dates from approximately a decade ago, with several review studies [24] and prototypes developed for both cavity receivers [25] and external receivers [26]. Recent research focuses on the thermo-hydraulic design of the receiver ([27–30]) due to its significant exergy destruction (>68 %), compared to minimal contributions from turbines and compressors (less than 3 %) [17]. The microchannel receiver used in this work is based on the bladed receiver concept, aiming to reduce heat losses and gradually increase compactness. This involves matching the hydraulic diameter of the compact structure to the thermal requirements of the absorber panel, thereby ensuring adequate cooling of the panel without penalizing the pressure drop [1].

The conventional CSP scheme, when using a pressurized gas as HTF in the receiver, consists of an indirect coupling between the CRS and the S-CO_2 cycle, employing a PCHE between the supercritical CO_2 from the cycle and the pressurized gas from the solar subsystem [31]. However, direct coupling can be considered if the proposed S-CO_2 cycle layout [32] is adopted and the solar heat input is located downstream of the turbine, thus reducing the CO_2 pressure. Additionally, this scheme is suitable for employing the previously mentioned microchannel central solar receiver [33].

A previous study compares this direct coupling using a conventional recompression cycle with indirect coupling schemes using conventional recompression cycles, recompression with partial cooling, or recompression with intercooling [23]. The conclusions of this study were quite insightful, highlighting several key points: the LCOE is influenced by both the initial investment and the annual electricity production, with parasitic consumptions being a significant factor in the latter. Regarding the investment, the cost of the turbomachinery is very similar across all configurations; the most crucial factor is the number and size of the heat exchangers in the cycle, mainly the recuperators and the primary heat exchanger, included in the indirectly coupled configurations. Regarding parasitic consumptions, it is crucial to consider the blower's power consumption in the solar subsystem for indirectly coupled schemes. This blower requires substantial power, as it circulates very hot gas. In this sense, the direct coupling option is advantageous as the fluid is compressed at a lower temperature. Considering these factors, the scheme with the lowest LCOE corresponds to an indirect coupling

with a recompression S-CO_2 cycle with partial cooling, followed by the direct coupling option with a conventional recompression S-CO_2 cycle. Accordingly, this study aims to build on the previous research [23] by introducing, as a novelty, new schemes for the direct cycle configuration, as only conventional recompression has been considered thus far. This work demonstrates that introducing more complex S-CO_2 layouts can lead to greater overall efficiencies.

In the methodology section, three directly coupled S-CO_2 cycles are presented, all based on the concept of solar heat input downstream of the turbine: conventional recompression, recompression with partial cooling, and recompression with intercooling. Then, the design of the microchannel solar receiver directly coupled to the power cycle is described. This section also depicts the circular heliostat field, which provides concentrated solar radiation to the receiver under design point conditions. Section 3 of the methodology outlines the main design equations and assumptions. The last section of the methodology describes the economic model used to evaluate the three CSP plants. In the results section, the cycle net efficiency, optical efficiency, and receiver thermal efficiency are calculated, as well as an estimation of the investment and the LCOE for each plant.

2. Methodology

2.1. Layouts

A recompression layout has been selected as the baseline for this study, with two additional configurations being considered:

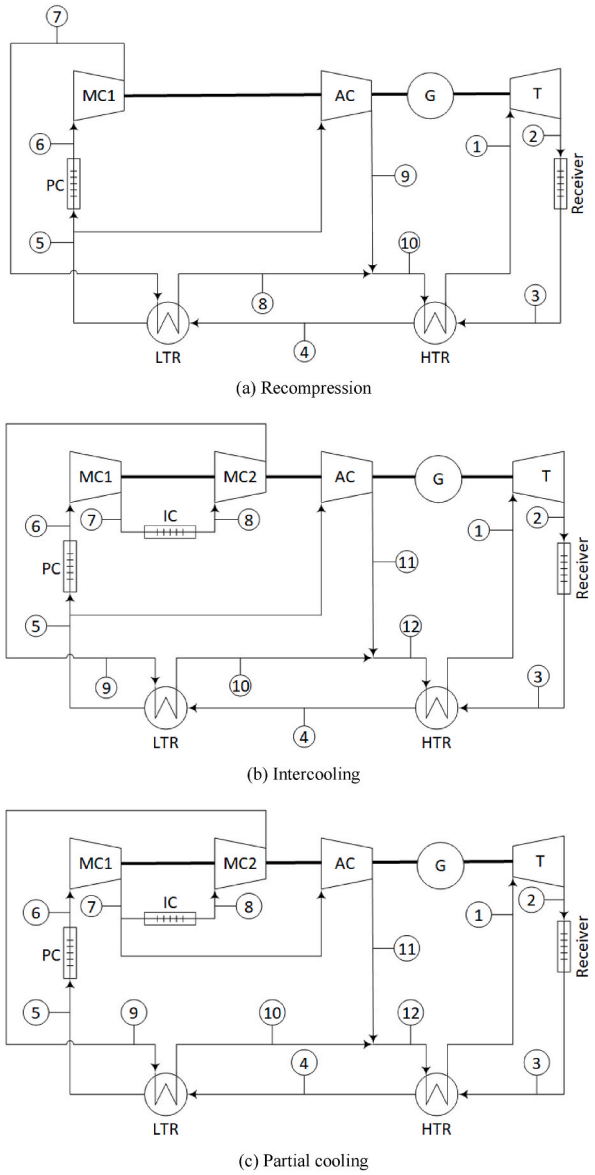

(a) Recompression

(b) Intercooling

(c) Partial cooling

Fig. 1. Considered layouts.

intercooling and partial cooling. Fig. 1 illustrates the three proposed layouts, while Fig. 2 displays their corresponding *T-s* diagrams. The central focus of the current study is the analysis of direct cycles, which are possible by shifting the heat input area from upstream to downstream of the turbine, as proposed by the authors in Ref. [32]. In this way, the receiver is connected to the low-pressure side of the power cycle, ranging between 96 bar and 75 bar in the current analysis. This shift results in the 2–3 line on the *T-s* diagrams, representing the heating of CO_2 in the solar receiver. This is followed by the 3–4 and 4–5 processes, during which the hot low-pressure CO_2 heats the cold high-pressure CO_2 in the high-temperature recuperator (HTR) and in the low-temperature recuperator (LTR), respectively.

The cycle net efficiency is defined in Equation (1), where the subscripts *PCfan* and *ICfan* stand for the fans of the precooler and the intercooler, as the power cycle releases heat directly into the environment (dry cooling). As the cycle is direct, there is no pumping

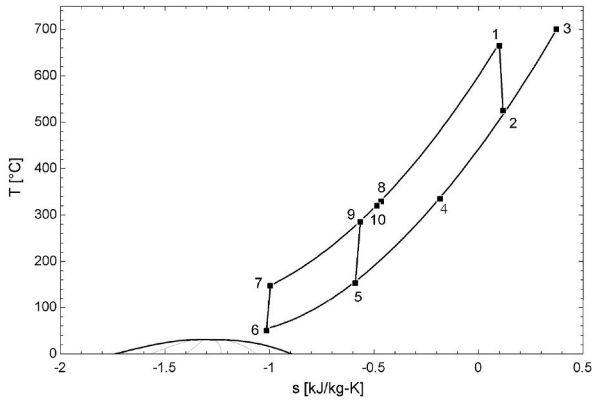

(a) Recompression

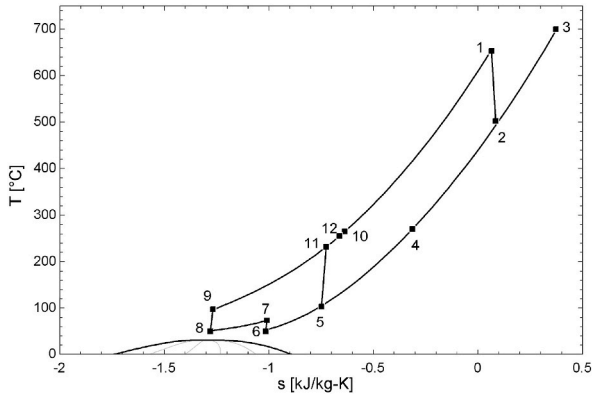

(b) Intercooling

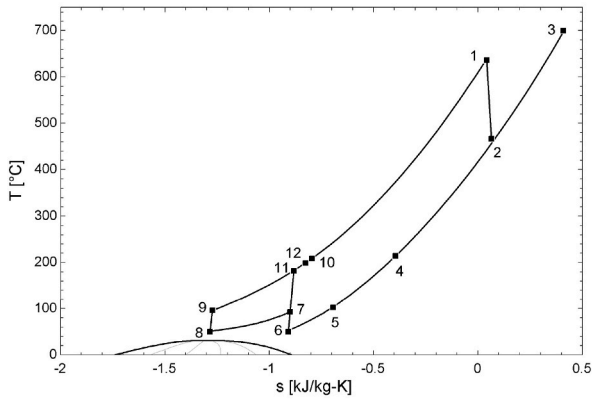

(c) Partial cooling

Fig. 2. *T-s* diagrams of considered layouts.

consumption for circulating the coolant in the solar receiver. Instead, the heat released in the receiver directly heats the working fluid of the power cycle. The net power of the plant is set to 50 MW_e in the three layouts.

$$\eta_{net-cycle} = \frac{\dot{W}_T - \dot{W}_{MC1} - \dot{W}_{MC2} - \dot{W}_{PCfan} - \dot{W}_{ICfan}}{\dot{Q}_{receiver}} \quad (1)$$

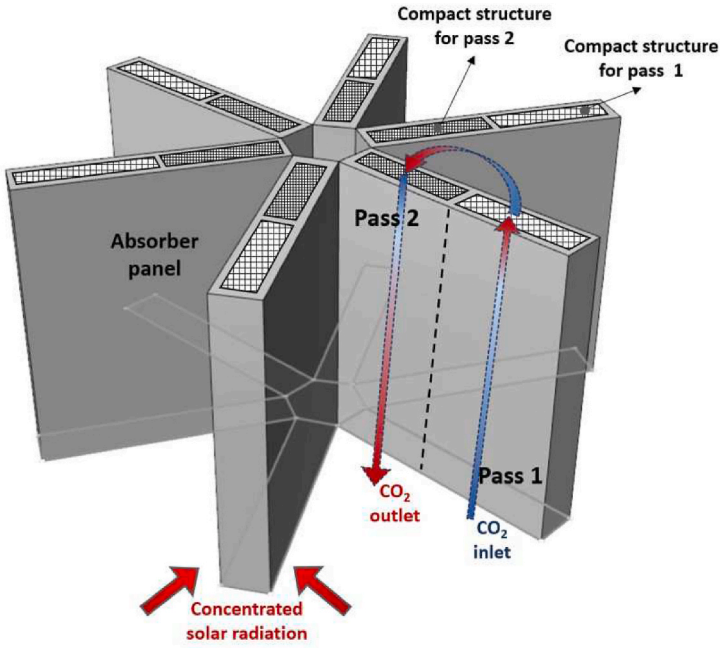

(a) Scheme of the microchannel central solar receiver for supercritical CO_2.

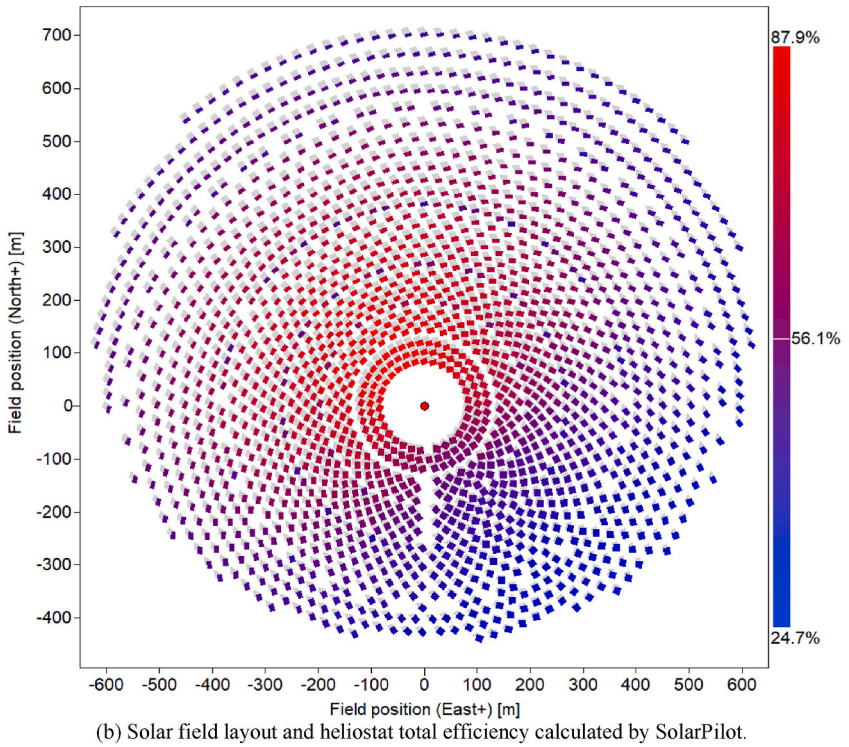

(b) Solar field layout and heliostat total efficiency calculated by SolarPilot.

Fig. 3. Central solar receiver (a) and heliostat field (b) coupled to each S-CO_2 cycle.

2.2. Solar field and receiver

The supercritical CO_2 from the cycle is heated in a microchannel central solar receiver, which has already been proposed and optimized in other works [33]. This receiver consists of compact structures performing as absorber panels arranged in a radial configuration, as depicted in Fig. 3a. The circular heliostat field, coupled to the solar receiver, has been calculated by means of SolarPilot software [34], as seen in Fig. 3b, and then exported to the Soltrace program [35] to accurately calculate the optical efficiency and the solar flux map on each absorber panel of the receiver.

The number of panels and other geometrical parameters of the receiver are defined by an optimization process that seeks to maximize the energy and exergy efficiencies (outlined in Equations (2)–(5)), considering both the heliostat field optics and the receiver thermal performance.

$$\eta_{en,solar\_field\ \&\ receiver} = \eta_{opt,solar\_field} \cdot \eta_{en,receiver} \tag{2}$$

$$\eta_{ex,solar\_field\ \&\ receiver} = \eta_{opt,solar\_field} \cdot \eta_{ex,receiver} \tag{3}$$

$$\eta_{en,receiver} = \frac{\dot{Q}_{th,HTF,receiver}}{\dot{Q}_{solar,receiver}} \tag{4}$$

$$\eta_{ex,receiver} = \frac{\Delta Ex_{HTF,receiver}}{\Delta Ex_{solar,receiver}} \tag{5}$$

In the above equations, $\dot{Q}_{th,HTF,receiver}$ and $\Delta Ex_{HTF,receiver}$ represent the thermal gain and the exergy gain of the HTF through the receiver, respectively; $\dot{Q}_{solar,receiver}$ is the concentrated solar radiation on the receiver, while $\Delta Ex_{solar,receiver}$ refers to the exergy associated to this solar radiation. The optimization process results in maximum exergy and energy efficiencies, which are the result of several opposing effects. For a specified thermal power, as the number of solar panels increases, the size of each panel decreases. This reduces the optical efficiency, due to the spillage loss, but enhances the energy efficiency, as heat losses are reduced due to a smaller aperture angle between two converging panels; it also increases the exergy efficiency, by both reducing the heat losses and the pressure drop, since the mass flow rate and the circuit length in each panel of the receiver decreases. This optimization process has been carried out for each of the three layouts considered, concluding that the optimum number of absorber panels is six, as shown in the results section.

Table 1
Equations to determine power consumptions by compressors and fans and power generation in the turbine, along with the boundary conditions and auxiliary methodology.

Component	Cycle	Power	Conditions and auxiliary equations	
MC1	RC	$\dot{m}\,(1-\alpha)(h_7-h_6)$	$0.88 = \frac{h_{7s}-h_6}{h_7-h_6}$	$p_6 = 85\ bar$ $T_6 = 50\ ^\circ C$
	ICL	$\dot{m}\,(1-\alpha)(h_7-h_6)$	$0.88 = \frac{h_{7s}-h_6}{h_7-h_6}$	$p_6 = 85\ bar$ $T_6 = 50\ ^\circ C\ p_7 = 115.3\ bar$
	PCL	$\dot{m}\,(h_7-h_6)$	$0.88 = \frac{h_{7s}-h_6}{h_7-h_6}$	$p_6 = 70.47\ bar$ $T_6 = 50\ ^\circ C\ p_7 = 115.9\ bar$
MC2	ICL	$\dot{m}\,(1-\alpha)(h_9-h_8)$	$0.88 = \frac{h_{9s}-h_8}{h_9-h_8}$	$T_8 = 50\ ^\circ C$
	PCL	$\dot{m}\,(1-\alpha)\,(h_9-h_8)$	$0.88 = \frac{h_{9s}-h_8}{h_9-h_8}$	$T_8 = 50\ ^\circ C$
AC	RC	$\dot{m}\,\alpha\,(h_9-h_5)$	$0.88 = \frac{h_{9s}-h_5}{h_9-h_5}$	
	ICL	$\dot{m}\,\alpha\,(h_{11}-h_5)$	$0.88 = \frac{h_{11s}-h_5}{h_{11}-h_5}$	
	PCL	$\dot{m}\,\alpha\,(h_{11}-h_7)$	$0.88 = \frac{h_{11s}-h_7}{h_{11}-h_7}$	
T	RC	$\dot{m}\,(h_1-h_2)$	$0.92 = \frac{h_1-h_2}{h_1-h_{2s}}$	$p_1 = 276.4\ bar$
	ICL	$\dot{m}\,(h_1-h_2)$	$0.92 = \frac{h_1-h_2}{h_1-h_{2s}}$	$p_1 = 300\ bar$
	PCL	$\dot{m}\,(h_1-h_2)$	$0.92 = \frac{h_1-h_2}{h_1-h_{2s}}$	$p_1 = 300\ bar$
PC Fan	RC	$\dot{m}_{aPC}\,v_a\left(\frac{0.065}{0.75}\right)$	$v_a = 0.8845\frac{m^3}{kg}$	
	ICL	$\dot{m}_{aPC}\,v_a\left(\frac{0.065}{0.75}\right)$	$v_a = 0.8845\frac{m^3}{kg}$	
	PCL	$\dot{m}_{aPC}\,v_a\left(\frac{0.065}{0.75}\right)$	$v_a = 0.8845\frac{m^3}{kg}$	
IC Fan	ICL	$\dot{m}_{aIC}\,v_a\left(\frac{0.065}{0.75}\right)$	$v_a = 0.8845\frac{m^3}{kg}$	
	PCL	$\dot{m}_{aIC}\,v_a\left(\frac{0.065}{0.75}\right)$	$v_a = 0.8845\frac{m^3}{kg}$	

2.3. Technical model and assumptions

Energy balances, boundary conditions, and auxiliary equations used to model the power cycles are shown in Tables 1 and 2, where numerical subscripts refer to Fig. 1, subscript *s* stands for a hypothetical isentropic point, and subscript *a* designates air properties (cooling medium). The subscripts *PC* and *IC* represent precooler and intercooler, respectively. Each cycle is designated as *RC* for recompression, *ICL* for intercooling, and *PCL* for partial cooling. Regarding the properties, *h* stands for enthalpy, *p* for pressure, *T* for temperature, C_p for specific heat at constant pressure, and *v* for specific volume. Finally, the main flow rate across the turbine is denoted as $\dot{m}$, modified by an α fraction in some compressors and heat exchangers.

The following pressures have been optimized to maximize the net cycle efficiency: the turbine inlet pressure for the three layouts; the main compressor (MC1) discharge pressure in both the intercooling and partial cooling layouts; and the turbine exhaust pressure in the partial cooling layout. Specifically, the turbine inlet pressure has been limited to 300 bar, a limit reached in both the intercooling and partial cooling layouts.

Printed circuit heat exchangers have been chosen for recuperators (LTR and HTR). In these exchangers, both fluid streams are CO_2, whose properties are strongly dependent on temperature and pressure, especially close to the critical point. To address this, an iterative procedure has been implemented, dividing the length of the heat exchanger into elements and assuming a continuous variation of properties [36]. Specific correlations have been developed for CO_2 convection heat transfer coefficients, which can be found in Ref. [37]. For the current analysis, the recommendations provided by Dostal [38] have been followed. PCHE dimensions have been obtained from Heatric [39], considering the manufacturing limitations due to its modularity. The maximum dimensions for a module are 0.6 m × 0.6 m x 1.5 m (width x length x height), with the height determining the flow path of the streams. Each module contains 96,000 channels (48,000 for each stream). A maximum of 14 modules can be piled up in parallel within a bonding structure to constitute the largest stack (8.4 m long). The inner channels are semi-circular, with a diameter of 2 mm and a pitch of 2.5 mm. Each layer of channels is 1.5 mm wide.

The pre-cooler (PC) and intercooler (IC) are cross-flow compact heat exchangers with a sCF-734 core. The air side has been modeled using the correlations implemented in Engineering Equation Solver (EES), revision 11.626, as the rest of the elements of the three cycles (except the receiver) with the main equations summarized in Tables 1 and 2 On the CO_2 side of the heat exchanger, the same discretization procedure as in the PCHEs has been applied, due to the proximity of this stream to the critical point in the pre-cooler (PC) and intercooler (IC).

Equation (6) gives the overall efficiency, from solar radiation to net electricity.

$$\eta_{overall} = \eta_{opt,solar\_field} \bullet \eta_{en,receiver} \bullet \eta_{net\_cycle} \tag{6}$$

The receiver thermal model is based on a Thermal Resistance Model (TRM) that characterizes the fluid heating along the flow direction. To determine the heat loss, it is necessary to calculate the absorber's external surface temperature. Thus, an additional model is needed to characterize the heat transfer through the panel thickness between parallel channel rows.

Table 2
Equations to determine heat transfer in the heat exchangers and receiver, along with the boundary conditions and auxiliary methodology.

Component	Cycle	Heat duty	Conditions and auxiliary equations	
Receiver	RC	$\dot{m}\,(h_3 - h_2)$	$T_3 = 700\,^{\circ}C$	$p_2 - p_3 = 6.11$ bar
	ICL	$\dot{m}\,(h_3 - h_2)$	$T_3 = 700\,^{\circ}C$	$p_2 - p_3 = 5.06$ bar
	PCL	$\dot{m}\,(h_3 - h_2)$	$T_3 = 700\,^{\circ}C$	$p_2 - p_3 = 4.60$ bar
HTR	RC	$\dot{m}\,(h_3 - h_4) = \dot{m}\,(h_1 - h_{10})$	$T_4 - T_{10} = 15\,^{\circ}C$	$p_4 = 0.98 \bullet p_3$ $p_1 = 0.98 \bullet p_{10}$
	ICL	$\dot{m}\,(h_3 - h_4) = \dot{m}\,(h_1 - h_{12})$	$T_4 - T_{12} = 15\,^{\circ}C$	$p_4 = 0.98 \bullet p_3$ $p_1 = 0.98 \bullet p_{12}$
	PCL	$\dot{m}\,(h_3 - h_4) = \dot{m}\,(h_1 - h_{12})$	$T_4 - T_{12} = 15\,^{\circ}C$	$p_4 = 0.98 \bullet p_3$ $p_1 = 0.98 \bullet p_{12}$
LTR	RC	$\dot{m}\,(h_4 - h_5) = \dot{m}\,(1-\alpha)(h_8 - h_7)$	$T_5 - T_7 = 5.5\,^{\circ}C$ $T_4 - T_8 = 5.5\,^{\circ}C$	$p_5 = 0.98 \bullet p_4$ $p_8 = 0.98 \bullet p_7$ $p_8 = p_9 = p_{10}$
	ICL	$\dot{m}\,(h_4 - h_5) = \dot{m}\,(1-\alpha)(h_{10} - h_9)$	$T_5 - T_9 = 5.5\,^{\circ}C$ $T_4 - T_{10} = 5.5\,^{\circ}C$	$p_5 = 0.98 \bullet p_4$ $p_{10} = 0.98 \bullet p_9$ $p_{10} = p_{11} = p_{12}$
	PCL	$\dot{m}\,(h_4 - h_5) = \dot{m}\,(1-\alpha)(h_{10} - h_9)$	$T_5 - T_9 = 5.5\,^{\circ}C$ $T_4 - T_{10} = 5.5\,^{\circ}C$	$p_5 = 0.98 \bullet p_4$ $p_{10} = 0.98 \bullet p_9$ $p_{10} = p_{11} = p_{12}$
PC	RC	$\dot{m}\,(1-\alpha)(h_5 - h_6) = \dot{m}_{aPC}\,C_{pa}\,20$	$C_{pa} = 1.006\,\frac{kJ}{kg \bullet K}$	$p_6 = 0.98 \bullet p_5$
	ICL	$\dot{m}\,(1-\alpha)(h_5 - h_6) = \dot{m}_{aPC}\,C_{pa}\,20$	$C_{pa} = 1.006\,\frac{kJ}{kg \bullet K}$	$p_6 = 0.98 \bullet p_5$
	PCL	$\dot{m}\,(h_5 - h_6) = \dot{m}_{aPC}\,C_{pa}\,20$	$C_{pa} = 1.006\,\frac{kJ}{kg \bullet K}$	$p_6 = 0.98 \bullet p_5$
IC	ICL	$\dot{m}\,(1-\alpha)(h_7 - h_8) = \dot{m}_{aIC}\,C_{pa}\,20$	$C_{pa} = 1.006\,\frac{kJ}{kg \bullet K}$	$p_8 = 0.98 \bullet p_7$
	PCL	$\dot{m}\,(1-\alpha)(h_7 - h_8) = \dot{m}_{aIC}\,C_{pa}\,20$	$C_{pa} = 1.006\,\frac{kJ}{kg \bullet K}$	$p_8 = 0.98 \bullet p_7$

For the energy balance along the flow direction, the channel is divided into Heat Control Elements (HCEs), where fluid properties are assumed to be constant. For each HCEs, the energy balance is described by Equations (7) and (8), and Equation (9) summarizes the heat losses.

$$\dot{Q}_{solar}|_{HCE} = \dot{Q}_{abs}|_{HCE} + \dot{Q}_{loss,ref}\big|_{HCE} \tag{7}$$

$$\dot{Q}_{abs}|_{HCE} = \dot{Q}_{conv,HTF}\big|_{HCE} + \dot{Q}_{loss,conv}\big|_{HCE} + \dot{Q}_{loss,rad}\big|_{HCE} \tag{8}$$

$$\dot{Q}_{loss}|_{HCE} = \dot{Q}_{loss,rad}\big|_{HCE} + \dot{Q}_{loss,ref}\big|_{HCE} + \dot{Q}_{loss,conv}\big|_{HCE} \tag{9}$$

The CO_2 heating along the absorber panel is characterized by the convection heat gain and the pressure drop in the flow direction. Both effects depend on the fluid regime: laminar, turbulent, or transitional. The equations used are summarized in Table 3.

In Table 3, Nu is the Nusselt number; Re_{Dh} is the Reynolds number based on the hydraulic diameter of the duct, D_h; Pr is the Prandtl number at the fluid temperature; and Pr_{is} is the Prandtl number based on the duct's inner surface temperature; L is the HCE length; ρ is the average fluid density; u is the average fluid velocity; and f_D is the Darcy friction factor, which is four times the Fanning friction factor, f_F.

In addition to the previous model, the temperature gradient between parallel channel rows in the absorber panel is modeled using an equivalent overall thermal resistance, as given by Equation (10). The specific values for each of these resistances are provided in Table 4.

$$R_{th,panel} = R_{p0,cond} + \frac{N_{c,rows}}{2}\left[R_{p,cond} + \left\{R_{c,conv} \parallel \left(R_{f,cond} + \left(\left(R_{f,cond} + R_{c,conv}\right) \parallel R_{f,conv}\right)\right)\right\} + R_{HTF}\right] \tag{10}$$

In Table 4, t_p represents the intermediate plate thickness (t_{p0} for the frontal plate); t_f and l_f denote the fin thickness and length, respectively, of the fin core in the compact structure; L_{HCE} and W_{HCE} are the HCE length and width, respectively. Finally, k_{rec} is the absorber thermal conductivity.

Both models, which simulate the receiver's thermal performance, have been implemented in Matlab [40] and are explained and validated in Ref. [41].

2.4. Economic model

The estimation of investment costs, which encompasses both direct and indirect expenses, has been carried out based on the framework outlined in Ref. [42]. Here, indirect costs are assumed to be 25 % of the direct costs, a standard not applied to the tower, receiver, and solar field, which will be addressed separately. Direct expenses are categorized into on-site costs, which include costs for purchased equipment, installation, piping, instrumentation, controls, and electrical gear (referred to as ONSC), and off-site costs, encompassing expenses for land, civil engineering, and service infrastructure (referred to as OFFSC). In the absence of specific scaling laws, the actual cost (C) cost is adjusted using Equation (11), which relies on the base cost (C_0), the base magnitude (M_0), the actual magnitude (M), and the escalation factor (a).

$$C = C_0 \bullet \left(\frac{M}{M_0}\right)^a \tag{11}$$

For calculating the costs related to the power cycle, reference is made to a recompression cycle study by Sandia National Laboratory for a 10 MWe setup [43]. This reference suggests a methodology for translating purchased-equipment costs (PEC) to on-site costs by a

Table 3
Correlations for the convection heat transfer coefficient (h_{conv}) and friction factor of the fluid in each heat control element (Source [33]).

Convection heat transfer: $\dot{Q}_{conv,HTF} = A_{channel} \cdot h_{conv} \cdot (T_{is} - T_f)$	
Correlation	Validity
$Nu_{Dh} = \dfrac{(f/8)\cdot(Re_{Dh}-1000)\cdot Pr}{1+12.7\cdot\left(\sqrt{\frac{f}{8}}\right)\cdot(Pr^{2/3}-1)}\cdot\left(\dfrac{Pr}{Pr_{is}}\right)^{0.11}$ $f = \left(1.82\cdot log_{10}(Re_{Dh}) - 1.64\right)^{-2}$	$5000 \le Re_{Dh}$
$Nu_{Dh} = 4.089 + \dfrac{Nu_{Gnielinski}\|_{Re=5000} - 4.089}{5000-2300}\cdot(Re-2300)$	$2300 < Re_{Dh} < 5000$
$Nu = 4.089$	$Re_{Dh} \le 2300$
Pressure drop: $\Delta P_{HTF} = \dfrac{1}{2}\cdot f_D \cdot \left(\dfrac{L_{HCE}}{D_h}\right)\cdot\rho\cdot u^2, f_D = 4\cdot f_F$	
Correlation	Validity
$\dfrac{1}{f_F} = 1.7372\cdot\ln\left[\dfrac{Re_{Dh}}{1.964\cdot ln(Re_{Dh}) - 3.8215}\right]$	$10^4 \le Re_{Dh} \le 10^7$
$f_F = f_{F,2300} + \dfrac{\left(f_F\|_{Re=10000} - f_F\|_{Re=2300}\right)\cdot(Re-2300)}{10000-2300}$	$2300 < Re_{Dh} < 10^4$
$f_F = \dfrac{16}{Re_{Dh}}$	$Re_{Dh} \le 2300$

Table 4
Thermal resistances included in the calculation of the thermal gradient across the panel thickness (Source [33]).

Symbol	Expression
$R_{p,cond}$	$R_{p,cond} = \frac{t_p}{k_{rec} \cdot W_{HCE} \cdot L_{HCE}}$
$R_{c,conv}$	$R_{c,conv} = \frac{1}{h_{conv} \cdot W_{HCE} \cdot L_{HCE}}$
$R_{f,cond}$	$R_{f,cond} = \frac{\left(\frac{l_f}{2}\right)}{k_{rec} \cdot t_f \cdot L_{HCE}}$.
$R_{f,conv}$	$R_{f,conv} = \frac{1}{2 \cdot l_f \cdot h_{conv} \cdot L_{HCE}}$
R_{HTF}	$R_{HTF} = \frac{1}{\rho \cdot C_p \cdot u \cdot W_{HCE} \cdot L_{HCE}}$

factor of 2.19. The scaling of PEC for key components is outlined as follows.

a) Printed circuit heat exchangers. Their costs are scaled based on module count, with the module serving as the manufacturing unit. An escalation factor of 0.4 [42] is applied, with a base PEC of 5 M€ for the HTR (having 4.46 modules) and 3 M€ for other exchangers, each with 3.1 modules [43]. The distinction arises due to the HTR's requirement for Inconel 617 alloy to withstand higher temperatures, unlike the SS 316 material for other exchangers [44].
b) The base cost for air-cooled heat exchangers (specifically the precooler and intercooler) is set at 836,500 €. This figure is for a high-pressure SS 316 exchanger with a 1000 m^2 inner area (bare tube), applying an escalation factor of 0.526 based on Matches' engineering estimate [45].
c) Turbomachinery and generator. Cost escalation is derived from Ref. [46], calculated using three distinct factors represented in Equations (12)–(14), with the final PEC determined by Equation (15).

$$f_W = \left(\frac{W}{10\ MW}\right)^{0.68} \tag{12}$$

$$f_p = \left(\frac{p\ [bar]}{200}\right)^{-0.6} \tag{13}$$

$$f_T = \frac{3.35 + \left(\frac{T[^\circ C]}{1{,}000}\right)^{7.8}}{3.35 + \left(\frac{650\ ^\circ C}{1{,}000}\right)^{7.8}} \tag{14}$$

$$PEC_{TMG}[M€] = f_W \bullet f_p \bullet f_T \bullet 6 \tag{15}$$

The cost of the tower, receiver, and heliostat field has been estimated by means of the SolarPilot software [34]. The on-site cost of the tower is scaled with the tower height (h_{tower}, m), according to Equation (16); the fixed tower cost is 3 M€, and the tower cost scaling exponent is equal to 0.0113. The on-site cost of the receiver is calculated by scaling a reference cost with the ratio of the current receiver area (A_{rec}, m^2) to the reference receiver area, applying a scaling exponent, according to Equation (17); the receiver reference cost is 103 M€, the receiver reference area is 1571 m^2 and the scalation factor is equal to 0.7. Finally, the on-site cost of the heliostat field is linearly scaled with a specific cost of 145 €/m^2 for the heliostat reflective area, as outlined in Equation (18). Off-site costs are estimated based on 16 €/m^2 for site improvements and 24,710 €/ha for land cost. Specific ratios for contingencies and other indirect costs are implemented in the software.

$$ONSC_{tower}[M€] = 3 \bullet e^{0.0113 \bullet h_t[m]} \tag{16}$$

$$ONSC_{receiver}[M€] = 103 \bullet \left(\frac{A_{rec}[m^2]}{1571}\right)^{0.7} \tag{17}$$

$$ONSC_{heliostat\_field}[M€] = 145 \bullet A_{heliostat\_field}\left[m^2\right] \tag{18}$$

The LCOE has been used as an economic indicator, based on the formulation of Bejan [42] outlined in Equation (19), where P stands for the annual electricity production (109.5 GWh assuming a capacity factor of 25 %) and $C_{0,OM}$ denotes the current cost of operation and maintenance, assumed to be 23 €/MWh [23]. The capital recovery factor (CRF) is defined in Equation (20) as a function of the weighted average capital cost (wacc) set at 8 % and the lifespan of the plant established at 30 years [23]. Finally, the cost escalation levelization factor ($CELF_{OM}$) is described in Equation (21), where the index k_{OM} is defined in Equation (22), being r_{OM} the nominal rate of escalation for operation and maintenance costs. Such nominal rate has been assumed to be zero, resulting in a $CELF_{OM}$ equal to one.

$$LCOE = \underbrace{\frac{FCI \bullet CRF}{P}}_{CAPEX} + \underbrace{C_{0,OM} \bullet CELF_{OM}}_{OPEX} \tag{19}$$

$$CRF = \frac{wacc \bullet (1+wacc)^N}{(1+wacc)^N - 1} \tag{20}$$

$$CELF_{OM} = \left[\frac{k_{OM} \bullet \left(1 - k_{OM}^N\right)}{1 - k_{OM}}\right] \bullet CRF \tag{21}$$

$$k_{OM} = \frac{1 + r_{OM}}{1 + wacc} \tag{22}$$

3. Results and discussion

Table 5 presents the properties of the state points in the analyzed layouts, while Table 6 details their energy performance. Three main parameters illustrated in Tables 5 and 6 influence the efficiency of the solar subsystem, defined as the combined optical efficiency of the solar field and the energy efficiency of the receiver (Equation (2)). Firstly, the cycle net efficiency impacts on the thermal power required from the solar subsystem: the higher the thermal efficiency, the lower the power required for the cycle to produce a net power of 50 MW_e. In this way, the highest cycle net efficiency is reached in the intercooling cycle (45.66 %), followed by the partial cooling (43.29 %), and finally, the recompression cycle (42.5 %). The lower thermal power requirement results in a lower tower height and a smaller receiver surface area, thereby increasing the receiver energy efficiency by minimizing the heat loss surface area, in addition to reducing investment costs. However, as can be seen in Table 6, a smaller receiver means higher spillage loss, thus decreasing optical efficiency.

Fig. 4 illustrates the variation in the efficiencies of both cooling cycles relative to the recompression cycle, according to Equation (23), where the superscript *X* stands for either *ICL* or *PCL*. Fig. 4a presents the results for the intercooling cycle, where the cycle's net efficiency increases by 7.44 % compared to the recompression cycle. This increase leads to a 1.81 % improvement in the receiver's energy efficiency and a 5.31 % reduction in the solar subsystem's optical efficiency, yielding an overall efficiency increase of 3.58 %. In contrast, Fig. 4b shows that for the partial cooling cycle, the lower increase in cycle net efficiency (1.86 %) results in a smaller increase in the receiver's energy efficiency (0.99 %) and a lower reduction in the solar subsystem's optical efficiency (3.51 %), leading to an overall efficiency reduction of 0.74 %.

$$\frac{\Delta\eta_{overall}^X}{\eta_{overall}^{RC}} = \frac{\Delta\eta_{opt,solar\_field}^X}{\eta_{opt,solar\_field}^{RC}} + \frac{\Delta\eta_{en,receiver}^X}{\eta_{en,receiver}^{RC}} + \frac{\Delta\eta_{net\_cycle}^X}{\eta_{net\_cycle}^{RC}} \tag{23}$$

The second parameter impacting solar subsystem performance is the required temperature increase in the solar receiver. In this case, the highest temperature rise is observed in the partial cooling configuration (233.8 °C), with the lowest in the recompression (174.7 °C) and an intermediate value for the intercooling configuration (197.3 °C). A greater thermal increase in the receiver reduces the volume of heat transfer fluid required, hence decreasing receiver dimensions, although the absorber surface area is the smallest for the intercooling layout, followed by the partial cooling and the recompression, as shown later in Table 7. This effect mirrors the previously mentioned factor: while the receiver energy efficiency increases, its optical efficiency decreases. Finally, the third factor is the average working temperature in the receiver, which is related to the thermal rise when the upper limit temperature is fixed (700 °C). Therefore, the receiver from the partial cooling cycle shows the lowest average working temperature, followed by the receiver from the intercooling layout and finally, the receiver from the recompression cycle. The operating temperature does not directly affect the receiver dimensions but leads to lower heat losses and, consequently, higher energy efficiency.

Table 5
Properties and state points of considered layouts.

Point	Recompression			Intercooling			Partial Cooling		
	T [°C]	p [bar]	h [kJ/kg]	T [°C]	p [bar]	h [kJ/kg]	T [°C]	p [bar]	h [kJ/kg]
1	665	276.4	669.2	652.9	300	653	636	300	631.3
2	525.3	96.42	506.6	502.7	95.37	479.7	466.2	79.47	438.1
3	700	90.31	721.1	700	90.31	721.1	700	74.87	721.9
4	335	88.5	284.1	270.1	88.5	209.9	213.9	73.38	150.9
5	152.9	86.73	75.31	102.8	86.73	11.76	102	71.91	21.78
6	50	85	−80.9	50	85	−80.9	50	70.47	−53.54
7	147.4	287.8	−20.01	73.7	115.3	−68.47	92.51	115.9	−29.06
8	329.5	282	244.5	50	113	−159	50	113.6	−160.1
9	284.8	282	186.3	97.27	312.4	−122.8	96.54	312.4	−124.3
10	320	282	232.3	264.6	306.1	154.9	208.4	306.1	74.8
11	–	–	–	231.9	306.1	109.2	182	306.1	33.75
12	–	–	–	255.1	306.1	141.8	198.9	306.1	60.38

Table 6
Energy performance of considered layouts.

	Recompression	Intercooling	Partial Cooling
MC1 power consumption [MW]	26.37	4.02	9.96
MC1 mass flow rate [kg/s]	433.04	323.73	406.9
MC2 power consumption [MW]	0	11.71	9.46
MC2 mass flow rate [kg/s]	0	323.73	264.00
AC power consumption [MW]	12.81	12.66	8.98
AC mass flow rate [kg/s]	115.46	129.87	142.9
T Power generation [MW]	89.18	78.62	78.65
T mass flow rate [kg/s]	548.5	453.6	406.9
Fan PC power consumption [kW]	257.7	114.3	116.8
Fan IC power consumption [kW]	0	111.6	131.8
Receiver heat absorbed [MW]	117.64	109.51	115.50
Net power [MW]	50	50	50
Solar subsystem optical efficiency [%]	81.77	77.43	78.90
Receiver energy efficiency [%]	87.74	89.33	88.61
Cycle net efficiency [%]	42.50	45.66	43.29
Overall efficiency [%]	30.49	31.58	30.26

As previously explained, the average entropic supply and rejection temperatures [42] in each cycle influence the net efficiency and, consequently, the performance of the solar subsystem and receiver. The average entropic temperature is defined in a fluid stream exchanging heat, without pressure drop, from inlet (i) to outlet (o) by Equation (24) [42]. Such a process is internally reversible, so considering that the enthalpy variation is the heat supplied per unit mass (q), Equation (25) is obtained. Equation (26) gives the average entropic temperature of heat supply, whereas Equation (27) gives the average entropic temeprature of heat rejection in recompression cycle and Equation (28) in both intercooling and partial cooling cycles.

$$\overline{T}_{io} = \frac{h_o - h_i}{s_o - s_i} \tag{24}$$

$$q = \overline{T}_{io} \bullet (s_o - s_i) \tag{25}$$

$$\overline{T}_{HS} = \frac{h_3 - h_2}{s_3 - s_2} \tag{26}$$

$$\overline{T}_{HR} = \frac{h_5 - h_6}{s_5 - s_6} \tag{27}$$

$$\frac{\dot{Q}_{PC} + \dot{Q}_{IC}}{\overline{T}_{HR}} = \frac{\dot{Q}_{PC}}{\overline{T}_{56}} + \frac{\dot{Q}_{IC}}{\overline{T}_{78}} \tag{28}$$

In an internally reversible cycle, the relative heat rejection (δ) is defined by Equation (29). This parameter represents the energy losses of the power cycle to the environment relative to the heat input. Equation (30) analyzes the variation of these parameters in the intercooling or partial cooling compared to the recompression cycle, in a similar way to Equation (23). Fig. 5a shows the results of the intercooling cycle. The average heat supply temperature remains nearly constant compared to the recompression cycle. In contrast, the average heat rejection temperature decreases by 7.06 %, leading to a 7.05 % reduction in energy losses (and an increase in the cycle efficiency). Fig. 5b analyzes the partial cooling cycle. In this case, the reduction in the average heat rejection temperature is less than in the intercooling cycle (6.03 % vs. 7.06 %), but the average heat supply temperature reduces significantly (1.93 %). This results in a smaller reduction in energy losses and, therefore, a lower cycle efficiency. Although this analysis assumes an internally reversible cycle behavior, similar trends are expected.

$$\delta = \frac{\dot{Q}_{HR}}{\dot{Q}_{HS}} = \frac{\overline{T}_{HR}}{\overline{T}_{HS}} \tag{29}$$

$$\frac{\Delta\delta^X}{\delta^{RC}} = \frac{\Delta\overline{T}^X_{HR}}{\overline{T}^{RC}_{HR}} - \frac{\Delta\overline{T}^X_{HS}}{\overline{T}^{RC}_{HS}} = \frac{\Delta\overline{T}^X_{HR}}{\overline{T}^{RC}_{HR}} + \frac{-\Delta\overline{T}^X_{HS}}{\overline{T}^{RC}_{HS}} \tag{30}$$

Considering all the aforementioned factors, it is found that the recompression and partial cooling layouts exhibit similar overall efficiencies (30.49 % and 30.26 %, respectively), with the intercooling layout showing the highest overall efficiency (31.58 %).

Table 7 presents the dimensions used to obtain the investment for the solar field, receiver, and heat exchangers. Table 8 details the fixed capital investment for the solar field and receiver in each layout, split into direct and indirect costs. Fig. 6 shows the variation of the investment in each component for the intercooling and the partial cooling cycles compared to the recompression cycle. It is clearly seen that the highest cost reductions occur in the receiver, with more significant reductions in the intercooling cycle. These substantial reductions are due to the temperature rise (233.8 °C in the partial cooling cycle, 197.3 °C in the intercooling cycle, and 174.7 °C in the

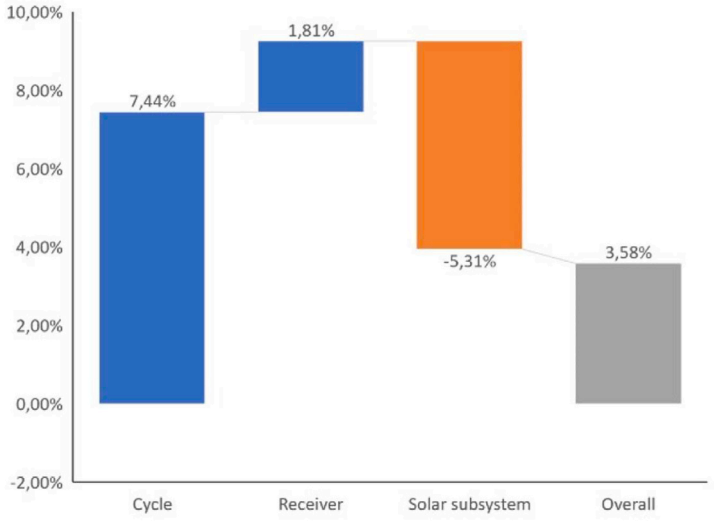

(a) Efficiency variation in the intercooling cycle compared to the conventional recompression cycle.

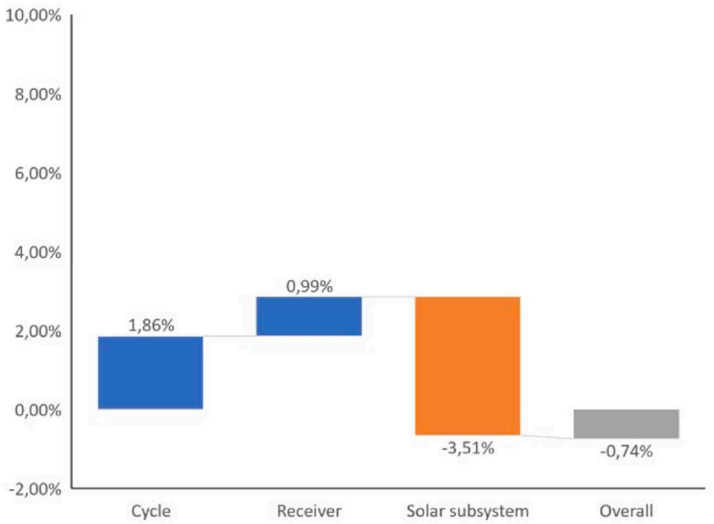

(b) Efficiency variation in the partial cooling cycle compared to the conventional recompression cycle.

Fig. 4. Efficiency variation breakdown in the intercooling (a) and partial cooling (b) cycles, compared to the recompression cycle.

Table 7
Dimensions of the main components used to assess the investment.

	Recompression	Intercooling	Partial cooling
Tower height [m]	112.6	110.2	112.3
Receiver absorber area [m^2]	367.5	255.1	280.5
Number of heliostats [−]	1563	1550	1607
HTR [modules]	28	22	22
LTR [modules]	60	65	52
PC heat transfer area [m^2]	4259	2856	2877
IC heat transfer area [m^2]	0	4256	3929

recompression cycle), which determines a mass flow rate reduction (406.9 kg/s, 453.6 kg/s, and 548.5 kg/s, respectively). However, the lower pressure in the partial cooling layout (74.87 bar at the outlet compared to 90.31 bar in the other layouts) slightly increases the receiver area and, consequently, the investment.

Finally, Table 9 summarizes the overall investment of the power plant, showing the final LCOE. Fig. 7 plots these results. The trend

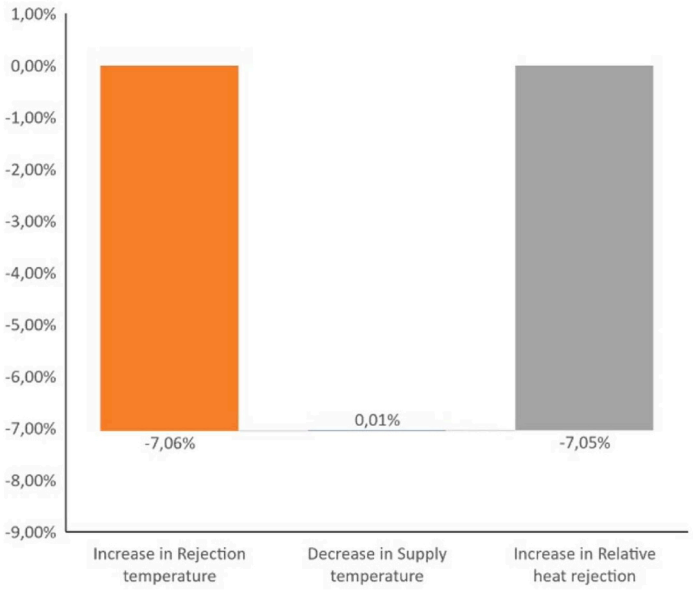

(a) Relative heat rejection variation in the intercooling cycle compared to the conventional recompression cycle.

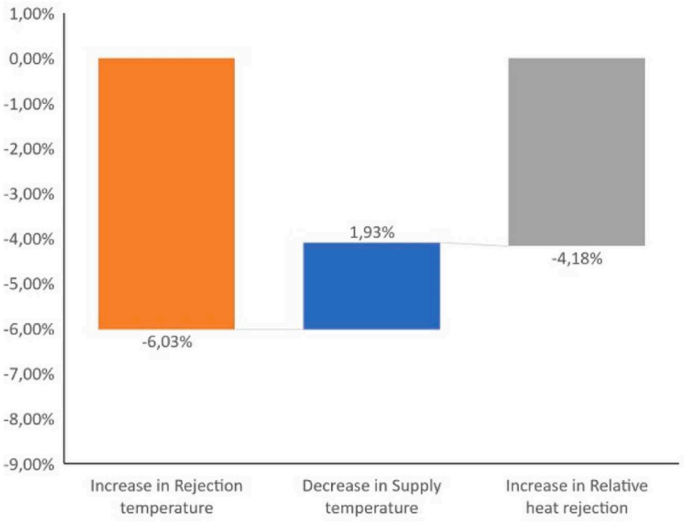

(b) Relative heat rejection variation in partial cooling cycle regarding recompression.

Fig. 5. Relative heat rejection variation breakdown in the intercooling (a) and in the partial cooling (b) cycles, compared to the conventional recompression cycle.

established by the temperature rise in the receiver is mirrored in the heat recuperation CAPEX: the higher the temperature rise, the lower the investment needed in recuperators. Another significant difference between the three layouts is the heat release system, which demands higher investments in the intercooling and precooling layouts. Although less heat is released, the average CO_2 temperature is closer to the ambient temperature (Fig. 5), thus requiring a larger heat transfer area. Finally, as previously discussed, a relevant difference in CAPEX occurs in the solar subsystem. The lowest LCOE is achieved in the intercooling layout, closely followed by the partial cooling layout.

The trend exhibited by the LCOE is not the same as the trend observed in overall efficiencies: while recompression and partial cooling achieve very similar efficiencies, intercooling and partial cooling result in very similar LCOE. This is explained by the significant influence of the solar subsystem on the LCOE. Intercooling and partial cooling have similar solar subsystem costs, both of which are lower than that of recompression. This similitude is due to the comparable efficiencies of the solar subsystem in the intercooling and partial cooling layouts (69.17 % and 69.91 %, respectively). However, the high cycle net efficiency achieved by the

Table 8
Investment for the solar subsystem.

Investment [M€]	Recompresssion	Intercooling	Partial cooling
Tower	10.702	10.483	10.669
Receiver	18.628	14.429	15.418
Site improvements	3.611	3.581	3.712
Heliostats field	32.720	32.448	33.642
Contingencies	4.698	4.289	4.511
Total direct cost	70.358	65.229	67.951
Land cost	3.752	3.514	3.654
Sales tax	2.872	2.623	2.758
Total indirect cost	6.624	6.136	6.412
Total Fixed Capital Investment	76.982	71.365	74.363

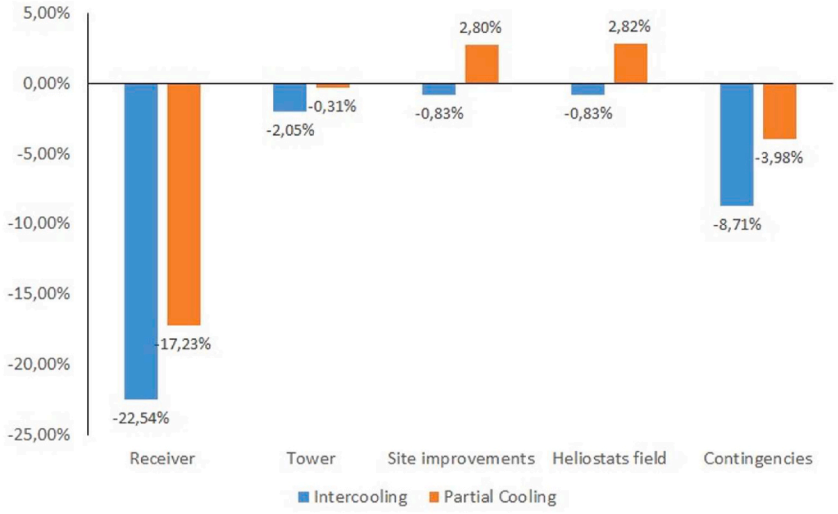

Fig. 6. Relative investment of the solar subsystem in the intercooling and partial cooling cycles compared to the conventional recompression cycle.

Table 9
Summary of the investment and resulting levelized cost of electricity.

Fixed Capital Investment (FCI) [M€]	Recompression	Intercooling	Partial Cooling
HTR	28.4	25.8	25.8
LTR	26.7	27.6	25.3
PC	4.9	4.0	4.0
IC	0.0	4.9	4.7
TM	40.3	38.3	38.2
Solar field and Receiver	77.0	71.4	74.4
Total FCI [M€]	177.3	171.9	172.3
Specific FCI [€/kW]	3546	3439	3446
CAPEX [€/MWh]	143.81	139.47	139.78
OPEX [€/MWh]	23.00	23.00	23.00
LCOE [€/MWh]	166.81	162.47	162.78

intercooling layout results in the highest overall efficiency. Although the recompression cycle exhibits a lower cycle net efficiency (42.5 %), this is offset by its high solar subsystem efficiency (71.75 %). In the same way, the high cycle net efficiency of partial cooling (43.29 %) is compensated by its relatively lower solar subsystem efficiency (69.91 %).

4. Conclusions

Three direct power cycles connected to a pressurized gas receiver have been analyzed. The use of direct cycles eliminates the need for an intermediate heat exchanger between the solar subsystem and the cycle, thereby saving costs. Additionally, the parasitic losses associated with pumping the heat transfer fluid in the receiver-primary heat exchanger loop are suppressed, thus improving the cycle net efficiency. A modified architecture in the S-CO_2 cycle proposed by the authors in previous works has allowed the elimination of the primary heat exchanger, converting the cycle working fluid into the receiver heat transfer fluid. The previous design of the receiver has

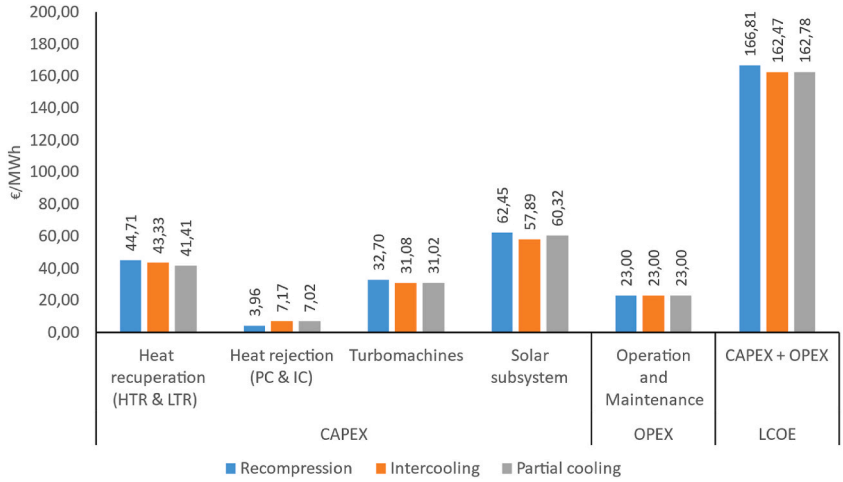

Fig. 7. Breakdown of LCOE

been demonstrated to be suitable for this novel layout. The absorber panels are based on compact structures ideal for pressurized gases and supercritical fluids, such as, in this case, CO_2.

The receiver coupled to a conventional recompression cycle operates at the highest average working temperature, followed by the intercooling cycle and the partial cooling cycle. This higher working temperature leads to greater heat losses and lower energy efficiency. For the energy efficiency calculation, the thermal power required for each receiver must also be taken into account, which is inversely proportional to the cycle efficiency and determines the absorber surface area. These considerations indicate that the receiver coupled to the intercooling cycle shows the highest energy efficiency, followed by the partial cooling cycle and, finally, the conventional recompression cycle. From an economic perspective, the receiver cost is proportional to its area. Again, the minimum cost is reached in the intercooling layout, followed by the partial cooling cycle. Although a larger receiver area generally leads to higher optical efficiency and a reduction in the number of heliostats, this lower heliostat field cost does not change the investment costs hierarchy shown for the receiver. Still, it is also valid for the complete solar subsystem.

The overall efficiency is similar in the three analyzed layouts, ranging from 30.26 % in the partial cooling cycle to 31.58 % in the intercooling cycle. This similarity is due to different trends in the three components of overall efficiency: cycle net efficiency, optical efficiency of the solar subsystem, and receiver energy efficiency. An increase in cycle net efficiency reduces the size of the receiver, which in turn increases the receiver energy efficiency but decreases the optical efficiency. The three layouts exhibit significant differences in the cycle net efficiency, ranging from 42.5 % in the recompression layout to 45.66 % in the intercooling layout. Regarding the solar subsystem (solar field and receiver), the recompression layout achieves the best performance, with a combined optical and energy efficiency of 71.75 %, compared to 69.17 % and 69.91 % for intercooling and partial cooling layouts, respectively. This superior performance of the solar subsystem in the recompression case is due to its larger receiver, which, however, increases its cost.

The LCOE ranges from 162.47 €/MWh in the intercooling layout to 166.81 €/MWh in the recompression layout, representing a difference of less than 3 %. This small variation is due to opposing trends in key factors. In conclusion, in the absence of thermal storage, there is no significant difference in LCOE, making the recompression layout preferable due to its simplicity. It is important to note that this comparison study does not consider a TES system, as all CSP plants have been analyzed at design conditions. However, TES is crucial because one of the main advantages of solar energy, compared to other renewable sources, is its dispatchability. In the analyzed CSP plant scheme, different types of TES could be considered. As with all of them, the temperature rise in the receiver reduces the storage medium inventory. The inclusion of thermal storage might favor the partial cooling layout.

CRediT authorship contribution statement

José Ignacio Linares: Writing – original draft, Supervision, Investigation, Funding acquisition, Conceptualization. **Eva Arenas:** Writing – review & editing, Supervision, Funding acquisition, Formal analysis, Conceptualization. **Maria José Montes:** Writing – original draft, Supervision, Methodology, Formal analysis, Conceptualization. **Alexis Cantizano:** Writing – review & editing, Methodology, Conceptualization. **José Rubén Pérez-Domínguez:** Writing – original draft, Methodology, Conceptualization. **José Porras:** Visualization, Methodology, Conceptualization.

Declaration of competing interest

The authors declare that they have no known competing financial interests or personal relationships that could have appeared to influence the work reported in this paper.

Data availability

Data will be made available on request.

Acknowledgments

Grant “Advanced integration of combined cycles in solar thermal power plants” (PID2019-110283RB-C33 and PID2019-110283RB-C31), funded by MCIN/AEI/10.13039/501100011033.

References

[1] M.J. Montes, A. Rovira, J. González-Aguilar, M. Romero, Solar Receiver Consisting of Absorber Panels Based on Compact Structures, 2022. Spanish Patent ES2911108. PCT application n. PCT/ES2022/070705. Eu. application n. 2023/10572.
[2] Ministry for Ecology Transition and Demographic Challenge, National Integrated Energy and Climate Plan 2021-2030 (in Spanish). https://www.miteco.gob.es/content/dam/miteco/es/ministerio/planes-estrategias/plan-nacional-integrado-energia-clima/plannacionalintegradodeenergiayclima2021-2030_tcm30-546623.pdf..
[3] National Commission of Markets and Competence, Report about the result of the third and fourth auctions to give the economic regime of renewable energies, done in October 25 and November 22, 2022, and its effect in the working of the electricity market and in the support of renewable energies, Files SUB/DE/003/22 and SUB/DE/004/22 (2023) (in Spanish), https://www.cnmc.es/sites/default/files/4872899.pdf.
[4] Ministry for Ecology Transition and Demographic Challenge, Royal Decree Law 8/2023, December 23, 2023, about measurements to tackle the economic and social consequences derived from clashes in Ukrain and Near East, as well as to mitigate the draught effects (in Spanish). https://www.boe.es/buscar/act.php?id=BOE-A-2023-26452..
[5] C.S. Turchi, Z. Ma, J. Dyreby, Supercritical carbon dioxide power cycle configurations for use in concentrating solar power systems, in: volume 5: manufacturing materials and metallurgy; marine; microturbines and small turbomachinery; supercritical CO2 power cycles. Presented at the ASME Turbo Expo 2012: Turbine Technical Conference and Exposition, American Society of Mechanical Engineers, Copenhagen, Denmark, 2012, pp. 967–973, https://doi.org/10.1115/GT2012-68932.
[6] Meng-Jie Li, Ming-Jia Li, Z. Ma, F. Yuan, Comparisons of thermal performance and cost for three thermal energy storage systems utilized in supercritical CO2 Brayton cycle, Energy Proc. 158 (2019) 4696–4701, https://doi.org/10.1016/j.egypro.2019.01.734.
[7] S. Trevisan, R. Guédez, B. Laumert, Supercritical CO2 Brayton power cycle for CSP with packed bed TES integration and cost benchmark evaluation, in: ASME 2019 Power Conference. Presented at the ASME 2019 Power Conference, American Society of Mechanical Engineers, Salt Lake City, Utah, USA, 2019, https://doi.org/10.1115/POWER2019-1903. V001T06A010.
[8] E. Johnson, L. Bates, A. Dower, P.C. Bueno, R. Anderson, Thermal energy storage with supercritical carbon dioxide in a packed bed: modeling charge-discharge cycles, J. Supercrit. Fluids 137 (2018) 57–65, https://doi.org/10.1016/j.supflu.2018.03.009.
[9] A. Sathishkumar, M. Cheralathan, Influence of functionalized graphene nanoplatelets on the phase transition performance of DI water-based NEPCMs for cool thermal storage systems, Energy Sources, Part A Recovery, Util. Environ. Eff. 45 (2022) 1187–1203, https://doi.org/10.1080/15567036.2021.2007312.
[10] A. Sathishkumar, M. Cheralathan, Influence of functionalized carbon flake on phase change characteristics of deionized (DI) water for cool thermal storage system, Fullerenes, Nanotub. Carbon Nanostruct. 30 (2022) 958–968, https://doi.org/10.1080/1536383X.2022.2050704.
[11] M. Mehos, C. Turchi, J. Vidal, M. Wagner, Z. Ma, C. Ho, W. Kolb, C. Andraka, A. Kruizenga, Concentrating solar power Gen3 demonstration roadmap, No. NREL/TP–5500-67464, 1338899), https://doi.org/10.2172/1338899, 2017.
[12] J. Yin, Q. Zheng, Z. Peng, X. Zhang, Review of supercritical CO2 power cycles integrated with CSP, International Journal of Energy Resources 44 (2020) 1337–1369, https://doi.org/10.1002/er.4909.
[13] M.T. White, G. Bianchi, L. Chai, S.A. Tassou, A.I. Sayma, Review of supercritical CO2 technologies and systems for power generation, Appl. Therm. Eng. 185 (2021) 116447, https://doi.org/10.1016/j.applthermaleng.2020.116447.
[14] K. Wang, M.-J. Li, J.-Q. Guo, P. Li, Z.-B. Liu, A systematic comparison of different S-CO2 Brayton cycle layouts based on multi-objective optimization for applications in solar power tower plants, Appl. Energy 212 (2018) 109–121, https://doi.org/10.1016/j.apenergy.2017.12.031.
[15] T. Neises, C. Turchi, Supercritical carbon dioxide power cycle design and configuration optimization to minimize levelized cost of energy of molten salt power towers operating at 650 °C, Sol. Energy 181 (2019) 27–36, https://doi.org/10.1016/j.solener.2019.01.078.
[16] T. Neises, C. Turchi, A comparison of supercritical carbon dioxide power cycle configurations with an emphasis on CSP applications, Energy Proc. 49 (2014) 1187–1196, https://doi.org/10.1016/j.egypro.2014.03.128.
[17] R. Vasquez Padilla, Y.C.S. Too, R. Benito, W. Stein, Exergetic analysis of supercritical CO2 Brayton cycles integrated with solar central receivers, Appl. Energy 148 (2015) 348–365, https://doi.org/10.1016/j.apenergy.2015.03.090.
[18] M. Lin, C. Guo, Z. Li, D. Zhao, Y. Zhu, B. Wang, X. Xu, Impact of pipe resistance on performance of supercritical carbon dioxide Brayton cycle system, Case Stud. Therm. Eng. 60 (2024) 104711, https://doi.org/10.1016/j.csite.2024.104711.
[19] R. Singh, S.A. Miller, A.S. Rowlands, P.A. Jacobs, Dynamic characteristics of a direct-heated supercritical carbon-dioxide Brayton cycle in a solar thermal power plant, Energy 50 (2013) 194–204, https://doi.org/10.1016/j.energy.2012.11.029.
[20] R. Singh, A.S. Rowlands, S.A. Miller, Effects of relative volume-ratios on dynamic performance of a direct-heated supercritical carbon-dioxide closed Brayton cycle in a solar-thermal power plant, Energy 55 (2013) 1025–1032, https://doi.org/10.1016/j.energy.2013.03.049.
[21] M.M. Abdelghafar, M.A. Hassan, H. Kayed, Comprehensive analysis of combined power cycles driven by sCO2-based concentrated solar power: energy, exergy, and exergoeconomic perspectives, Energy Convers. Manag. 301 (2024) 118046, https://doi.org/10.1016/j.enconman.2023.118046.
[22] H.H. Zhu, K. Wang, Y.L. He, Thermodynamic analysis and comparison for different direct-heated supercritical CO2 Brayton cycles integrated into a solar thermal power tower system, Energy 140 (2017) 144–157, https://doi.org/10.1016/j.energy.2017.08.067.
[23] M.J. Montes, R. Guedez, J.I. Linares, M.A. Reyes-Belmonte, Advances in solar thermal power plants based on pressurised central receivers and supercritical power cycles, Energy Convers. Manag. 293 (2023) 117454, https://doi.org/10.1016/j.enconman.2023.117454.
[24] Q. Li, G. Flamant, X. Yuan, P. Neveu, L. Luo, Compact heat exchangers: a review and future applications for a new generation of high temperature solar receivers, Renew. Sustain. Energy Rev. 15 (2011) 4855–4875, https://doi.org/10.1016/j.rser.2011.07.066.
[25] S.M. Besarati, D.Y. Goswami, E.K. Stefanakos, Development of a solar receiver based on compact heat exchanger technology for supercritical carbon dioxide power cycles, J. Sol. Energy Eng. 137 (2015) 031018, https://doi.org/10.1115/1.4029861.
[26] S.D. Sullivan, J. Kesseli, J. Nash, J. Farias, D. Kesseli, W. Caruso, High-efficiency low-cost solar receiver for use ina a supercritical CO2 recompression cycle (No. DOE-BRAYTON–0005799, 1333813). https://doi.org/10.2172/1333813, 2016.
[27] Z.D. Zhang, K. Wang, Y.J. Liu, X. Zhang, Y.H. Fan, C.H. Min, Study on the convective heat transfer characteristics of supercritical CO2 in mini-channels under unilateral heating conditions for application in a compact solar receiver, Int. J. Heat Mass Tran. 219 (2024) 124839, https://doi.org/10.1016/j.applthermaleng.2023.120862.
[28] K. Wang, Y.J. Liu, Z.D. Zhang, X. Zhang, Y.H. Fan, C.H. Min, Three-dimensional shape optimization of fins for application in compact supercritical CO2 solar receivers, Int. J. Heat Mass Tran. 221 (2024) 125013, https://doi.org/10.1016/j.ijheatmasstransfer.2023.125013.
[29] R. Mochahari, A.K. Ray, K.R. Kumar, D. Rakshit, Thermal performance of a supercritical CO2 based central receiver, Mater. Today: Proc. 90 (Part 1) (2023) 56–60, https://doi.org/10.1016/j.matpr.2023.04.607.

[30] B.S. Emerick, F.G. Battisti, A.K. da Silva, Geometric optimization of a solar tower receiver operating with supercritical CO2 as working fluid, Appl. Therm. Eng. 228 (2023) 120318, https://doi.org/10.1016/j.applthermaleng.2023.120318.
[31] M.J. Montes, R. Guedez, D. D'Souza, J.I. Linares, Thermoeconomic analysis of concentrated solar power plants based on supercritical power cycles, Appl. Sci. 13 (2023) 7836, https://doi.org/10.3390/app13137836.
[32] J.I. Linares, M.J. Montes, A. Cantizano, C. Sánchez, A novel supercritical CO2 recompression Brayton power cycle for power tower concentrating solar plants, Appl. Energy 263 (2020) 114644, https://doi.org/10.1016/j.apenergy.2020.114644.
[33] M.J. Montes, R. Guédez, D. D'Souza, J.I. Linares, J. González-Aguilar, M. Romero, Proposal of a new design of central solar receiver for pressurised gases and supercritical fluids, Int. J. Therm. Sci. 194 (2023) 108586, https://doi.org/10.1016/j.ijthermalsci.2023.108586.
[34] M.J. Wagner, T. Wendelin, SolarPILOT: a power tower solar field layout and characterization tool, Sol. Energy 171 (2018) 185–196, https://doi.org/10.1016/j.solener.2018.06.063.
[35] T. Wendelin, SolTRACE: a new optical modeling tool for concentrating solar optics. Proceedings of the ISEC 2003: International Solar Energy Conference, 15-18 March 2003, Kohala Coast, Hawaii, American Society of Mechanical Engineers, New York, 2003, pp. 253–260. NREL Report No. CP-550-32866.
[36] I.P. Serrano, A. Cantizano, J.I. Linares, B.Y. Moratilla, Modeling and sizing of the heat exchangers of a new supercritical CO2 Brayton power cycle for energy conversion for fusion reactors, Fusion Eng. Des. 89 (2014) 1905–1908, https://doi.org/10.1016/j.fusengdes.2014.04.039.
[37] L.F. Cabeza, A. De Gracia, A.I. Fernández, M.M. Farid, Supercritical CO2 as heat transfer fluid: a review, Appl. Therm. Eng. 125 (2017) 799–810, https://doi.org/10.1016/j.applthermaleng.2017.07.049.
[38] V.A. Dostal, Supercritical Carbon Dioxide Cycle for Next Generation Nuclear Reactors, Massachusetts Institute of Technology (MIT), Cambridge, MA, USA, 2004. Doctoral Thesis.
[39] R. Le Pierres, D. Southall, S. Osborne, Impact of mechanical design issues on printed circuit heat exchangers, in: Proceedings of 3rd SCO2 Power Cycle Symposium 2011, University of Colorado at Boulder, CO, 2011. May 24-25.
[40] MATLAB & Simulink – MathWorks, 2022. https://matlab.mathworks.com.
[41] D. D'Souza, M.J. Montes, M. Romero, J. González-Aguilar, Energy and exergy analysis of microchannel central solar receivers for pressurised fluids, Appl. Therm. Eng. 219 (2023) 119638, https://doi.org/10.1016/j.applthermaleng.2022.119638.
[42] A. Bejan, G. Tsatsaronis, M.J. Moran, Thermal Design and Optimization, A Wiley-Interscience publication. Wiley, New York, 1996. ISBN: 978-0-471-58467-4.
[43] D. Fleming, T. Holschuh, T. Conboy, G. Rochau, R. Fuller, Scaling considerations for a multi-megawatt class supercritical CO2 Brayton cycle and path forward for commercialization, in: volume 5: manufacturing materials and metallurgy; marine; microturbines and small turbomachinery; supercritical CO2 power cycles. Presented at the ASME Turbo Expo 2012: Turbine Technical Conference and Exposition, American Society of Mechanical Engineers, Copenhagen, Denmark, 2012, pp. 953–960, https://doi.org/10.1115/GT2012-68484.
[44] D. Southall, R. Le Pierres, S.J. Dewson, Design considerations for compact heat exchangers. Proceedings of the 2008 International Congress on Advances in Nuclear Power Plants: ICAPP '08 : Embedded Topical Meeting, June 8-12, 2008, Anaheim, California, American Nuclear Society, La Grange Park, Ill, 2008.
[45] https://www.matche.com/equipcost/Exchanger.html.
[46] M.J. Driscoll, P. Hejzlar, 300 MWe supercritical CO_2 plant layout and design, MIT nuclear engineering department, report No: mit-GFR-014, Center for Advanced Nuclear Energy Systems MIT Nuclear Engineering Department (2004).